

# Protein crystallography with a novel large-area pixel detector

Gregor Hülsen,\*‡ Christian Broennimann, Eric F. Eikenberry and Armin Wagner¶

Paul Scherrer Institut, 5232 Villigen PSI, Switzerland. Correspondence e-mail: gregor.huelsen@pmodwrc.ch

The PILATUS 1M detector, developed at the Paul Scherrer Institut, is a single-photon-counting hybrid pixel detector designed for macromolecular crystallography. With more than 1 million pixels covering an area of  $243 \times 210$  mm, it is the largest such device constructed to date. The detector features a narrow point spread function, very fast readout and a complete absence of electronic noise. Unfortunately, this prototype detector has numerous defective pixels and sporadic errors in counting that complicate its operation. With appropriate experimental design, it was largely possible to work around these problems and successfully demonstrate the application of this technology to structure determination. Conventional coarse  $\phi$ -sliced data were collected on thaumatin and a refined electron density map was produced that showed the features expected of a map at  $1.6 \text{ \AA}$  resolution. The results were compared with the performance of a reference charge-coupled device detector: the pixel detector is superior in speed, but showed higher  $R$ -factors because of the counting errors. Complete fine  $\phi$ -sliced data sets recorded in the continuous-rotation mode showed the predicted advantages of this data collection strategy and demonstrated the expected reduction of  $R$ -factors at high resolution. A new readout chip has been tested and shown to be free from the defects of its predecessor; a PILATUS 6M detector incorporating this new technology is under construction.

© 2006 International Union of Crystallography  
Printed in Great Britain – all rights reserved

## 1. Introduction

Crystallography is the principal technique for determining macromolecular structures at atomic resolution and uses advantageously the high intensity of third-generation synchrotron X-ray sources (Sussman *et al.*, 1998). Macromolecular crystallography experiments benefit also from excellent beamline equipment, recent software advances and modern X-ray detectors (Gruner *et al.*, 2002; Plaisier *et al.*, 2003). However, the latter do not take full advantage of the brightness of modern synchrotron sources.

Among other attributes, an ideal detector for these experiments would have quantum-limited photon detection and a short readout time with no readout noise. Hybrid pixel-array detectors, originally developed for high-energy physics experiments, have the potential to meet these requirements (Gemme, 2003; Schnetzer, 2003). The technology of these detectors features a two-dimensional array of p–n diodes connected to a readout chip which is designed in complementary metal oxide semiconductor (CMOS) technology. In the design reported here, each pixel in the readout chip has a low-noise amplifier, a comparator and a digital counter. X-rays are recorded in single-photon counting mode and data are

thus stored digitally at the earliest possible stage. This architecture leads to several advantages over current detectors, as follows.

(i) The quantum efficiency (QE) of the detector is limited only by the absorption properties of the sensor. The QE of a  $300 \text{ }\mu\text{m}$  silicon sensor is 0.98 for 8 keV ( $1.5 \text{ \AA}$ ) X-rays, near the ideal limit of 1.0, but decreases for higher X-ray energies [0.73 for 12 keV ( $1.0 \text{ \AA}$ ) X-rays].

(ii) No detector noise is added to the signal.

(iii) Readout time is reduced to a few milliseconds.

(iv) The counting rates are matched to beam intensities at protein crystallography beamlines at third-generation synchrotrons.

(v) The detector is not sensitive to X-rays during readout; therefore no mechanical shutter is required.

(vi) The detector has a very sharp point spread function (PSF) of one pixel, which allows better resolution of adjacent reflections.

(vii) Low-energy X-rays can be suppressed by the comparator.

The technology also introduces some disadvantages. First, to cover a large area, a pixel detector is built of individual modules between which a small region is insensitive to X-rays (Fig. 1). Second, counting detectors have rate limitations, in contrast to integrating detectors, such as charge-coupled

‡ Present address: PMOD/WRC, 7270 Davos Dorf, Switzerland.

¶ Present address: Diamond Light Source Ltd, Chilton, UK.



**Figure 1**  
The PILATUS 1M detector. The sensitive surface of the detector is provided by 18 individual modules. The modules are tilted by  $6^\circ$  and overlap.

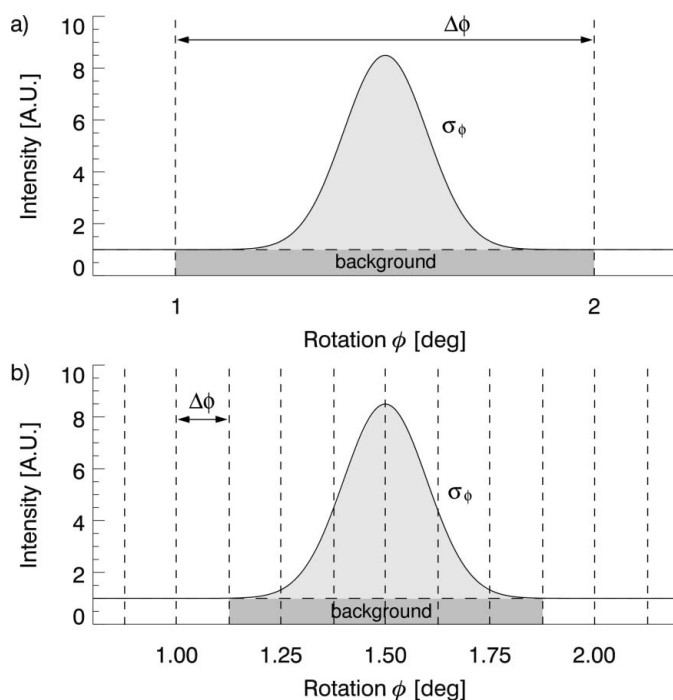


**Figure 2**  
Rocking curve of a Bragg reflection passing through the Ewald sphere with a width  $\sigma_\phi = 0.1^\circ$ . (a) The intensity of the reflection is sampled in one image with a rotation increment  $\Delta\phi = 1^\circ$  per image. (b) With finer sampling, the position of the reflection is much better defined and less background is included in the integration.

device (CCD) detectors or integrating pixel detector designs (Renzi *et al.*, 2002). Third, the better spatial resolution due to the sharp PSF is compromised by larger pixels. However, in crystallographic experiments, the separation of reflections can be increased by a larger sample to detector distance, thus requiring a larger number of pixels to acquire a high number of reflection orders. The larger distance reduces isotropic background radiation, which falls off by  $1/r^2$ , and therefore increases the signal to background ratio.

PILATUS 1M, the first large-area pixel detector, was designed for the protein crystallography beamline X06SA of the Swiss Light Source (SLS) at the Paul Scherrer Institut (PSI). The detector covers an area of  $243 \times 210$  mm with  $1120 \times 967$  pixels (Fig. 1). It operates in single-photon counting mode at room temperature and has noise-free readout in less than 5.9 ms. A description of the detector is given by Broennimann *et al.* (2006). The prototype detector suffers from two types of defects: (i) it contains a high number of dead pixels and (ii) the digital counter can switch into a random count state because of a subtle design fault (Appendix A). Despite these defects, which could be largely overcome by appropriate measuring techniques, the detector has been successfully used for protein crystallography and its potential could be demonstrated. In addition to conventional coarse  $\phi$ -sliced experiments, fine  $\phi$ -sliced data sets were recorded. In the absence of readout noise, the latter technique is proposed to improve data quality (Arndt, 1986; Dauter & Wilson, 2001). Furthermore, the short readout time decreases the time needed to collect data sets of several thousand images. The results of experiments performed with the PILATUS 1M detector were compared with the performance of two CCD detectors (Mar CCD165 and Mar CCD225, from Mar USA, Inc., Evanston, IL, USA).

### 1.1. Advantages of fine $\phi$ -slicing

One important step in the analysis of diffraction data is to separate the net intensity of the recorded Bragg reflections from the background radiation. The integrated intensity,  $I$ , of a reflection is the sum of counts of the pixels in the peak region,  $P$ , less the background,  $B$ . The background under the reflection is estimated in the recorded images from nearby pixels in the two dimensions of the detector plane and from pixels of the peak region at different rotation angles,  $\phi$ , of the crystal. The boundary between background and peak region is found by fitting a three-dimensional profile to the reflection (Diamond, 1969; Rossmann, 1979). The reflection profile is usually well represented in the detector plane but the rocking curve, *i.e.* the  $\phi$  profile of the reflection, is only coarsely sampled, as illustrated in Fig. 2(a). With the large rotation increment,  $\Delta\phi$ , of typically  $1^\circ$  per image, the reflection is recorded in one image and the peak position is poorly defined in this dimension. Because the reflection moves slightly in the two dimensions of the detector plane as it passes through the Ewald sphere (Pflugrath, 1999), the boundary of background and peak region is not well defined in all three dimensions. Therefore, the profiles are not fitted at the precise position of the reflections. A large rotation increment minimizes the number of images of a data set. However, reflections must not overlap in the plane of the detector. In fine  $\phi$ -slicing experiments, the rocking curve of the reflection is sampled more finely (Fig. 2b) and thus the position of the reflection is much better defined. In principle, the rotation increment  $\Delta\phi$  should be considerably smaller than the width of the rocking curve,  $\sigma_\phi$ , and it is recommended (Kabsch, 2005) to set the rotation increment to

$$\Delta\phi \simeq \frac{1}{5}\sigma_\phi. \quad (1)$$

The width of the rocking curve is usually expressed by the mosaicity of the crystal, which is the width of the reflecting range, as defined by Kabsch (1988). Throughout this paper we follow this definition of the crystal mosaicity. In fine  $\phi$ -sliced data, the mosaicity can be deduced from the standard deviation of the rocking curve as shown in Fig. 2(b) and in this case is  $0.1^\circ$ . As the rocking curve is not available in coarse  $\phi$ -sliced experiments, the mosaicity, reported by crystallographic integration programs, is a refinement parameter. In the example shown in Fig. 2, the rotation increment should be, according to equation (1), around  $0.02^\circ$  per image.

A minimum amount of background should be included in the integration because the variance of the background is added to the variance of the intensity of the Bragg reflection. As the measurement of X-rays is Poisson distributed, the standard deviation of the estimation of  $m$  photons is

$$\sigma(m) = m^{1/2}. \quad (2)$$

The standard deviation of the reflection intensity  $I = f(P, B)$  is

$$\sigma(I) = (P + B)^{1/2}. \quad (3)$$

The quality of the measurement can be defined by the ratio of the intensity to its standard error  $I/\sigma(I)$ :

$$I/\sigma(I) = I/(P + B)^{1/2}. \quad (4)$$

Therefore, the accuracy of a measurement is higher for lower background. In the first example described above, background from the left and right side of the reflection is unnecessarily included in the peak intensity (Fig. 2a), whereas in the fine  $\phi$ -sliced experiment this background can be excluded (Fig. 2b). Another consequence of equation (4) is that high-intensity reflections are less affected by background than low-intensity reflections. Finer  $\phi$ -slicing should therefore especially increase the data quality of weak reflections in the high-resolution shells, which should increase the quality of the structure determination. Furthermore, small anomalous differences, important for phasing in multiple- or single-wavelength anomalous diffraction experiments, would be measured with higher accuracy.

If pixels are significantly larger than the width of the reflection in the detector plane, unnecessary background is also collected. The background should in this case be decreased by increasing the specimen to detector distance, but this may require a larger detector.

### 1.2. Continuous-sample-rotation mode

Readout noise, added to each image by most detector technologies, prohibits fine  $\phi$ -sliced experiments (Pflugrath, 1999). In addition, a long dead time between exposures,  $t_d$ , makes these experiments very time consuming because the number of images is significantly increased. For many widely used detectors,  $t_d$  is a few seconds and is the sum of the readout time, the time needed for shutter synchronization and the data transfer time.

With the PILATUS 1M detector these experiments are performed using a novel data collection mode at synchrotrons: the crystal rotation is started and images are continuously recorded using the electronics of the detector as the shutter. Thus, the dead time of experiments with this detector is equal to its very short readout time and the utilization of both the detector and the X-ray source is significantly increased. Furthermore, synchronization with a mechanical shutter is no longer needed. However, without shutter operation the sample is not protected against radiation damage during the dead time. Therefore  $t_d$  should be small, as is the case for the PILATUS 1M detector. Fig. 3 shows a fine-sampled  $\phi$  profile of a reflection recorded with the PILATUS 1M detector in this data collection mode. Detector dead time scales the intensity but does not change the profile shape as long as enough sample points have been acquired [equation (1)]. Thus, fine  $\phi$ -slicing ensures that the  $\phi$  profiles can be reconstructed with full accuracy.

The times needed for experiments using the PILATUS 1M detector in this data collection mode or a CCD detector (Mar CCD165) can be compared. The PILATUS 1M detector has a readout time of 5.9 ms and no additional time is needed in the continuous-sample-rotation mode. With an exposure time of 1 s, 1.4 h are needed to perform a fine  $\phi$ -sliced experiment with 5000 images, while a conventional coarse  $\phi$ -sliced data set with 180 images is collected in 3 min. The CCD detector is normally operated with an overhead of 2.5 s. The synchronization of the shutter and goniometer adds approximately 0.5 s to this time, leading to a dead time of 3 s for this CCD detector. Thus, the fine  $\phi$ -slicing experiment takes five hours

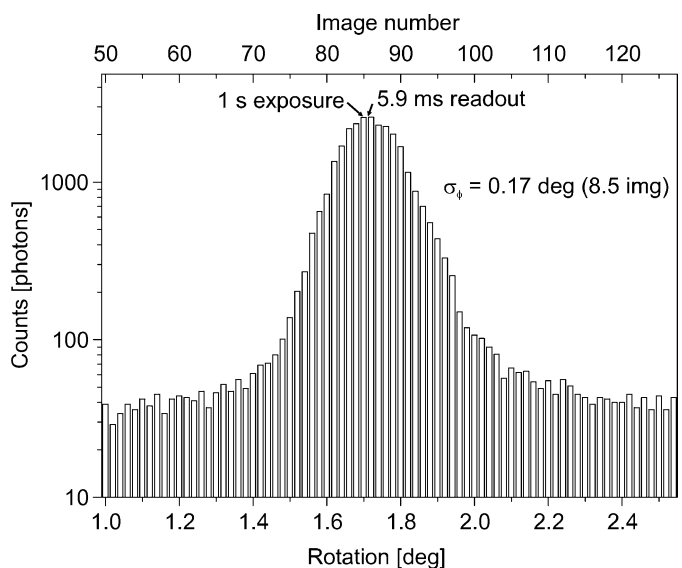


**Figure 3** Typical fine  $\phi$ -sliced profile on a logarithmic scale of a Bragg reflection as it passes through the Ewald sphere as measured with the PILATUS 1M detector with  $\Delta\phi = 0.02^\circ$  per image. The profile was redrawn to illustrate the continuous-sample-rotation mode of the detector: the dead time of 5.9 ms (not to scale), due to the readout of an image, leads to a 0.59% reduction of the measured intensity for the 1 s exposures. The sampling theorem ensures that the  $\phi$  profile can be reconstructed with full accuracy from the fine  $\phi$ -sliced data. The dead time between exposures therefore does not represent any loss of information.

and the coarse  $\phi$ -slicing experiment is finished in 12 min, using the identical exposure time of 1 s.

## 2. Methods

### 2.1. Experimental setup

All the data presented here were collected at the protein crystallography beamlines X06SA and X10SA of the SLS. The X-ray wavelength was 1.0 Å and the exposure times were 1 s, unless otherwise noted. Since the flux was too high for fine  $\phi$ -sliced experiments with this exposure time, the X-ray intensity was reduced by filters and beam-confining slits to 2% of the initial beam intensity. The PILATUS 1M detector was mounted on an additional translation stage, allowing horizontal positioning of the detector to micrometre precision, perpendicular to the central beam direction. The diffraction data were collected from flash-frozen (100 K) thaumatin and insulin crystals, obtained as described by Schulze-Briese *et al.* (2005). For the experiments performed with the pixel detector, two thaumatin crystals (#1 and #2) from the same batch were used. One thaumatin crystal (#3) from a different batch grown under the same conditions and one cubic Zn-free insulin crystal (#4, space group  $I2_13$ , crystal size  $180 \times 180 \times 140 \mu\text{m}$ ) were used in the experiments with the CCD detectors. In a fine  $\phi$ -sliced experiment, the insulin crystal was scanned five times. The rotation increment and the exposure time were decreased successively (0.5, 0.25, 0.1 and 0.05° per image with 10, 5, 2 and 1 s per image). The first scan was repeated at the end to monitor possible degradation of the crystal during the experiment.

For flatfield calibration, the detector was placed 90° with respect to the central beam direction to minimize patterns in the flatfield image caused by scattering by mechanical parts. At this position, the detector surface was illuminated with fluorescence X-rays (1.0 Å) from a solution of KBr. The images were collected at a sample to detector distance of 125 mm because the geometry of the PILATUS 1M detector causes this calibration to work best when the distance is the same as that used in the crystallographic experiments.

### 2.2. Data correction and processing

After the experiments, the images of the PILATUS 1M detector are corrected for flatfield inhomogeneity. Each image is multiplied with an intensity calibration file, *i.e.* flatfield corrected (Barna *et al.*, 1999; Broennimann *et al.*, 2004). The calibration file also blanks out unreliably counted pixels, resulting in 9% dead pixels in a corrected image.

The images need to be corrected for spatial distortion (Hülsen *et al.*, 2005). Within a module of the detector, the pixel positions are accurate to sub-micrometre precision because the sensor is fabricated with photolithographic processes. As the 300  $\mu\text{m}$  silicon sensor is much thicker than the thin phosphor screens of CCD detectors ( $\sim 30 \mu\text{m}$ ), a considerable parallax effect distorts the images. A parallax back transformation is carried out to determine the impinging position on the sensor surface. A second source of distortion is the

mechanical deviation of the modules from their assumed positions. Therefore, the pixel positions of each module are adjusted to the real position in space. A 6° tilt of the modules creates a shingled surface of the detector. To process the data with standard crystallographic software, the detector surface is projected onto a virtual plane in front of the detector. The parallax effect and the detector geometry require correction files for each experimental setup. After the distortion correction, the standard deviation of pixel positions from a perfect grid is 0.31 pixels.

The active area of the PILATUS 1M detector is reduced by the insensitive areas between modules. In addition, dead pixels are randomly distributed in the detector area. In Fig. 4(a), a section of a diffraction image recorded with the pixel detector is shown. The dead pixels are marked white. As reflections from diffraction experiments can only be integrated correctly if no dead pixel affects the peak profile, these dead pixels reduce the usable area significantly. Therefore data sets were recorded twice. First the total rotation range was scanned and after the detector translation, the second data set was recorded. The detector was translated by one pixel (217  $\mu\text{m}$ ) using the horizontal translation stage. By merging the two data sets, the dead area caused by pixel defects could be reduced to 3%. A pixel value of the corrected image (Fig. 4b) represents the average information of two measurements, or the value of one measurement if one pixel was dead, or zero if both were dead.

Fine  $\phi$ -sliced data sets could in addition be corrected for random counting errors (Appendix A). This is essential for these experiments because the significantly longer total exposure time increases the number of counting errors in the data. The errors can be detected to a certain degree in the  $\phi$  profiles of Bragg reflections (Fig. 5). A semiautomatic algorithm was developed which scans through the data and removes many of these errors. Each  $\phi$  profile is fitted to an average reflection profile in all three dimensions. Detected outliers are replaced by an average value of the neighbouring pixels. Despite this routine, an unknown number of errors remain, which cannot be detected (Fig. 5d).

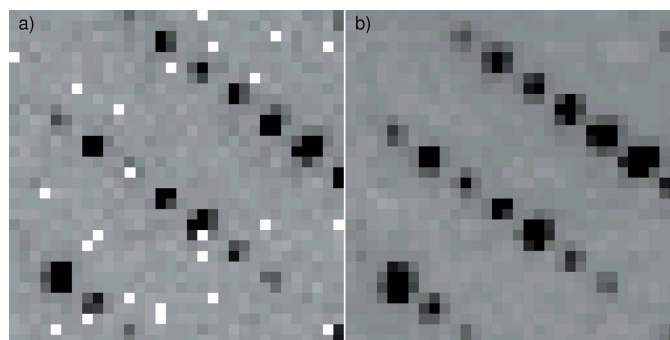


**Figure 4**  
A section of a diffraction image of a thaumatin crystal recorded with the PILATUS 1M detector. (a) The raw image with dead pixels (marked white). Reflections with such pixels in their neighbourhood must be excluded from the analysis. (b) The corrected image shows that dead pixels are successfully reduced by the detector translation procedure.

**Table 1**

Results of the analysis of thaumatin data for the coarse  $\phi$ -sliced experiments using two detector systems and a rotation increment  $\Delta\phi = 0.5^\circ$  per image.

The performance of the detectors in the highest resolution shell is listed in parentheses.

Detector	PILATUS 1M	Mar CCD165
Crystal	#1	#3
Crystal size ( $\mu\text{m}$ )	300 $\times$ 150 $\times$ 100	
Space group	92 ( <i>P4<sub>1</sub>2<sub>1</sub>2</i> )	
Unit-cell <i>a</i> , <i>c</i> ( $\text{\AA}$ )	57.50, 150.89	57.78, 150.06
Diffraction statistics		
Resolution ( $\text{\AA}$ )	70–1.6 (1.7–1.6)	
Completeness (%)	99.9 (99.9)	94.8 (68.4)
Unique reflections	34320 (5579)	32580 (3817)
Total observed reflections	258324 (41040)	300251 (29070)
Redundancy	7.53 (7.36)	9.22 (7.62)
$\sigma_{\text{spot}}$ (pixel)	0.50	0.32
$R_{\text{merge}}$ (%)	9.5 (36.0)	4.6 (13.0)
Mean $I/\sigma(I)$	13.02 (5.17)	33.78 (13.35)
Refinement statistics		
$R_{\text{cryst}}$ (%), working set	19.40	19.74
$R_{\text{free}}$ (%), free set	21.20	21.05

Using the *XDS* package (Kabsch, 1988; Kabsch, 1993) the data sets were indexed and the intensities of the reflections calculated and scaled. This crystallographic analysis package has been revised and could successfully analyze the large data sets of the fine  $\phi$ -sliced experiments.

The quality of the data sets is expressed by the reliability factor, or *R*-factor, which is defined as Drenth (1994)

$$R_{\text{merge}} = \frac{\sum_{hkl} \sum_i^{n_{hkl}} |I - I_{hkl,i}|}{\sum_{hkl} \sum_i^{n_{hkl}} I_{hkl,i}}, \quad (5)$$

where  $I_{hkl,i}$  is the intensity of the *i*th reflection out of a set of symmetry-related reflections *hkl* with multiplicity  $n_{hkl}$ . The ratios  $I/\sigma(I)$  are another indication of the quality of a data set.

### 3. Experimental results and discussion

#### 3.1. Coarse $\phi$ -sliced experiments

A conventional coarse  $\phi$ -sliced experiment on a thaumatin crystal (#1) was performed with the PILATUS 1M detector at beamline X06SA. A rotation range of  $120^\circ$  was measured using a rotation increment of  $0.5^\circ$  per image. Table 1 summarizes the results of the experiment.

The pixel detector collected the data with a completeness of 99.9%. This value could only be achieved by the translation technique described above. Loss of reflections, due to the insensitive area between the modules, was no problem for this high-symmetry crystal. The standard deviation of the reflection position ( $\sigma_{\text{spot}} = 0.5$  pixels) indicates that images could be spatial-distortion

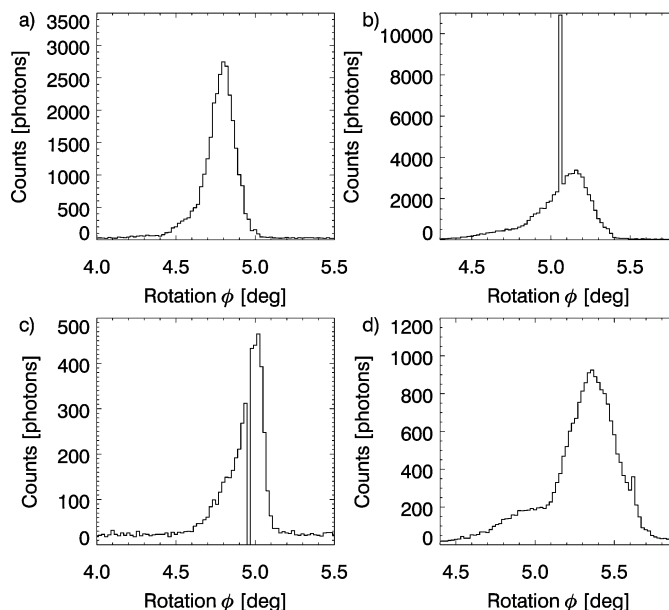


**Figure 5**  
 $\phi$  profiles of Bragg reflection recorded with the PILATUS 1M detector. (a) A typical reflection profile without error. (b), (c) Random counting errors can be detected and corrected if two conditions are fulfilled: many sample points have been acquired for the profile and the counting error is either unreasonably high or low. (d) The outlier at  $\phi = 5.62^\circ$  was not detected by the semiautomatic algorithm.

corrected to a sufficient degree. The value of the *R*-factor below 10% shows that the defects of the prototype could be successfully compensated by the correction procedures. But the low value of 13 for the signal to noise ratio indicates that counting errors affect the data quality.

From the data obtained, the structure of the protein could be solved by molecular replacement using a structure model obtained by the sulfur single-wavelength anomalous dispersion (S-SAD) method at beamline X06SA (Wagner, 2006). The subsequent isotropic refinement of the thaumatin structure against the measured diffraction data with the *Crystallography and NMR System (CNS)* (Brünger *et al.*, 1998) led to reasonable statistics (Table 1). In Fig. 6, a stereo plot of a section of the electron density map after the refinement is shown (blue:  $2F_o - F_c$ ; red:  $F_o - F_c$ ;  $2\sigma$  contour level;  $F_o$  and  $F_c$

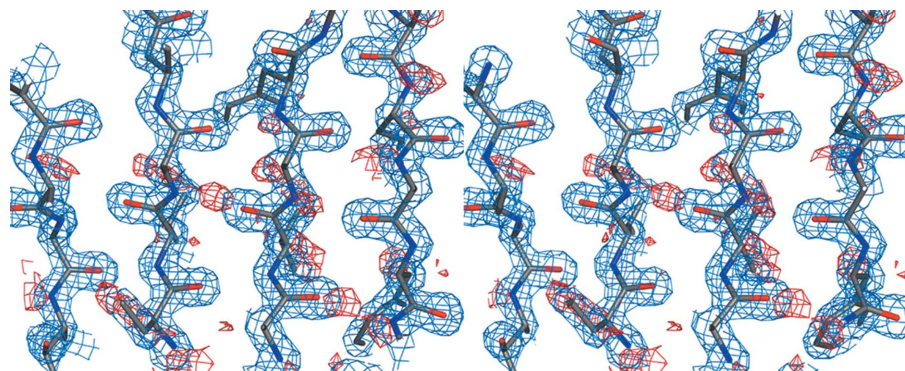


**Figure 6**  
Stereo plot of a section of the electron density map of thaumatin after refinement (blue:  $2F_o - F_c$ ,  $2\sigma$  contour level; red:  $F_o - F_c$ ,  $2\sigma$  contour level).

are observed and calculated structure factors). The map is relatively noisy, but shows all the features expected at 1.6 Å resolution.

The experiment was repeated with the Mar CCD165 detector, installed at beamline X06SA, using identical experimental parameters but a different thaumatin crystal (#3). This crystal did not diffract as well as the one used in the experiment with the pixel detector. This can be seen in the lower completeness of 68.4% in the highest resolution shell. However, the reliability factor and the signal to noise ratio of the data set are more than a factor of two better for the CCD detector. This result shows that with the counting errors, higher quality intensity measurements with the PILATUS 1M detector are not possible. The refinements of the thaumatin structure against the measured diffraction data obtained with the CCD and the PILATUS 1M detector led to nearly identical statistics (Table 1).

### 3.2. Fine $\phi$ -sliced experiments

Fine  $\phi$ -sliced data sets, containing 5200 images, were collected with the PILATUS 1M detector at beamline X06SA. The total rotation range of 104° was measured with a rotation increment of 0.02° per image. After the correction procedure (§2.2), the mosaicity of the thaumatin crystal (#2) was determined by *XDS* to be 0.2°, which corresponds well with the value of 0.17° deduced from the rocking curve shown in Fig. 3. To fulfill equation (1), the rotation increment of the data set was reduced to 0.04° image. This was done by adding pairs of images and scaling the resulting images down by a factor of two. Because of the absence of readout noise, this procedure resulted in a data set which is effectively identical to that of an experiment with a rotation increment of 0.04° per image. Two more data sets were prepared by adding sets of 5 and 25 images together with an appropriate scaling factor. The three resulting data sets thus have oscillation ranges of 0.04, 0.1 and 0.5° per image.

The reliability factors as a function of the resolution shell are shown in Fig. 7 and a summary of the finest and the coarsest data set is presented in Table 2. Compared with the performance of the detector in the conventional coarse  $\phi$ -

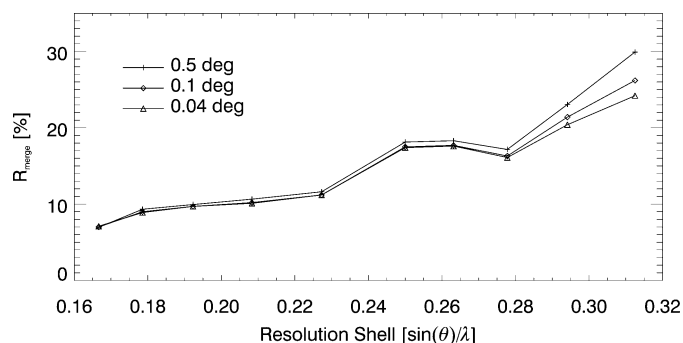


**Figure 7**  
*R*<sub>merge</sub> for data sets with decreasing rotation increments  $\Delta\phi$  collected with the PILATUS 1M detector. A thaumatin crystal was scanned with  $\Delta\phi = 0.02^\circ$  per image. The figure displays the quality of this data set summed to larger rotation increments. The quality increases with finer rotation increment.

**Table 2**

Results of the analysis of thaumatin data for the fine  $\phi$ -sliced experiments with the PILATUS 1M detector.

The performance of the detector in the highest resolution shell is listed in parentheses. The images with a rotation increment  $\Delta\phi = 0.02^\circ$  per image were summed to give images with rotation increments equivalent to 0.5 and 0.04° per image, respectively (see also Fig. 7 and text).

$\Delta\phi$ (° per image)	0.5	0.1	0.04
Crystal		#2	
Crystal size ( $\mu\text{m}$ )		300 × 150 × 100	
Space group		92 ( <i>P</i> <sub>4</sub> 2 <sub>1</sub> 2)	
Unit-cell <i>a</i> , <i>c</i> (Å)	57.60, 151.11	57.55, 150.86	57.55, 150.81
Diffraction statistics			
Resolution (Å)		70–1.6 (1.7–1.6)	
Completeness (%)	99.9 (99.8)	99.9 (100.0)	99.9 (100.0)
Unique reflections	34377 (5589)	34393 (5599)	34393 (5599)
Total observed reflections	218721 (30239)	245350 (39074)	245416 (39314)
Redundancy	6.36 (5.41)	7.13 (6.99)	7.14 (7.02)
$\sigma_{\text{spot}}$ (pixel)	0.59	0.64	0.74
<i>R</i> <sub>merge</sub> (%)	11.8 (34.0)	10.2 (26.2)	10.2 (24.2)
Mean <i>I</i> / $\sigma$ ( <i>I</i> )	13.09 (5.67)	13.28 (7.04)	12.36 (7.24)

sliced experiment (Table 1), the overall *R*-factor of the finest data set (0.04° per image) differs by only 0.7%. The higher number of counting errors due to the significant increase in exposure time could be successfully compensated by the correction algorithm (§2.2). The 10% better *R*-factor in the highest resolution shell indicates that weak reflections were much better acquired, which can however also be influenced by a difference in crystal quality.

Compared within the summed data sets, the data in the high-resolution shells were considerably improved (Fig. 7). The difference of the *R*<sub>merge</sub> values for the finest and the coarsest data set is 10% in the highest resolution shell. No significant improvement is observed in the low-resolution shells. Thus, the fine  $\phi$ -sliced data demonstrate the beneficial effect of this data acquisition mode for weak reflections in the high-resolution shells.

The reduction of the rotation increment per image leads to an increase in the effect of readout noise in data from CCD detectors. To verify this, a total rotation range of 30° was measured five times with one insulin crystal (#4) at beamline

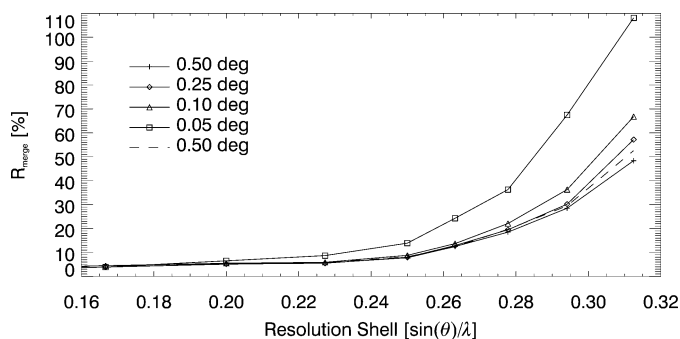


**Figure 8**  
*R*<sub>merge</sub> for experiments with decreasing rotation increments  $\Delta\phi$  performed with the CCD detector. An insulin crystal was scanned five times. The last scan (dashed line) with  $\Delta\phi$  equal to the first scan shows the degradation of the crystal. The quality of the data set decreases with finer  $\phi$ -slicing.

X10SA. The results of this experiment performed with the Mar CCD225 detector are shown in Fig. 8. The comparison of the performances of the two detectors reveals the principal differences of the two detector types: it can be seen that the advantages of finer slicing are compromised by the readout noise of the CCD, which leads to a significant increase of the *R*-factors for smaller rotation increments, especially in the high-resolution shells. This result is not caused by degradation of the crystal, which can be seen by comparing the first with the last scan. The angular rotation speed and beam flux were held constant during all scans to keep the experimental conditions constant.

The mosaicity of the crystal ( $\sim 0.1^\circ$ ) would require a  $\Delta\phi$  equal to  $0.02^\circ$  per image [equation (1)]. But because of the high *R*-factors already obtained at  $0.05^\circ$  per image, a further reduction of the rotation increment for finer  $\phi$ -slicing was not performed.

#### 4. Conclusions and outlook

The PILATUS 1M detector is the first large-area silicon pixel detector designed for macromolecular crystallography. The performance of the detector was successfully investigated with crystallographic experiments. One important advantage of this detector is its fast readout time: conventional crystallographic data sets can be collected in less than 3 min. The dead pixels of the prototype could be largely compensated by detector translation: with this technique a completeness of 99.9% was achieved for a high-symmetry crystal. No limiting effect of the insensitive area between modules of the detector was found. The analysis of the crystallographic data shows that with the correction procedures reasonable *R*-factors could be obtained, but random counting errors affect the data quality. However, the structure of the protein could be solved and the refined electron density map is of good quality.

The theoretically predicted advantages of finer rotation increments have been verified. In contrast to data from CCD detectors, the quality of the high-resolution data was increased by using a rotation increment smaller than the mosaic spread of the crystal. The duration of the experiments could be reduced by operating with continuous sample rotation, without a mechanical shutter.

The analysis of the performance of the PILATUS 1M detector provided critical information for the development of the next-generation pixel detector system. The readout chip of the new detector will be replaced by the significantly improved design of the PILATUS II chip. Outstanding data quality should be achieved, because the defects of the prototype chip have been eliminated in the new readout chip. A PILATUS 6M detector incorporating this new technology is under construction. With an expected framing rate of  $\sim 10$  Hz, fine  $\phi$ -sliced data sets can be recorded in the same time as conventional coarse  $\phi$ -sliced data sets are currently collected with CCD detectors. Furthermore, conventional data sets can potentially be collected in a few seconds in the continuous-rotation mode, depending on the experimental conditions.

#### APPENDIX A

##### Random counting errors

Because of a property of the counter design, random counting errors are possible when two X-ray photons arrive on a pixel within a short time interval, *e.g.* between  $t_1$  and  $t_2$ . Below that interval, the pixel electronics cannot resolve the two events and count a single event; at longer intervals, the electronics can separate the events clearly. X-ray arrival times follow the interval distribution (Evans, 1955). With a mean rate of photon arrival events per pixel,  $a$  ( $\gamma \text{ s}^{-1} \text{ pixel}^{-1}$ ), the average interval between events is  $1/a$ . The probability that the duration of a particular interval will be between  $t$  and  $t + dt$  is

$$dP_t = a \exp(-at) dt. \quad (6)$$

If  $N$  intervals are measured with  $q$  pixels, the number of intervals,  $n_c$ , between  $t_1$  and  $t_2$  is

$$n_c = Nq \int_{t_1}^{t_2} a \exp(-at) dt, \quad (7)$$

$$= Nq[\exp(-at_2) - \exp(-at_1)], \quad (8)$$

$$\simeq Nqa(t_2 - t_1), \quad at \ll 1. \quad (9)$$

If the probability is  $p$  that the counter switches into a random count state for a time interval between  $t_1$  and  $t_2$ , then the number of counting errors in an image is

$$n_e = pn_c. \quad (10)$$

In a homogeneously illuminated image of the PILATUS 1M detector with a 1 s exposure and an average counting rate of  $a = 2300 \gamma \text{ s}^{-1} \text{ pixel}^{-1}$ ,  $n_e = 50 \times 10^3$  counting errors were detected (5% of the pixels). The time interval in which counting errors are likely is estimated from chip design simulations to be between  $t_1 = 450$  ns and  $t_2 = 650$  ns. Thus, in the exposure described above  $n_c = 2300 \times 10^6 \times 2300 \times (650 - 450) \times 10^{-9} \simeq 10^6$  [equation (9)] and the probability,  $p$ , for a counting error is approximately 0.05.

For very low X-ray rates (background), a negligible number of counting errors occur ( $n_e = 16$  for  $a = 40 \gamma \text{ s}^{-1} \text{ pixel}^{-1}$ ), but an increasing number of counting errors occur at higher rates, as in strong reflections with several  $1000 \gamma \text{ s}^{-1} \text{ pixel}^{-1}$ .

Due to the counting errors, it is observed that the variance of intensity measurements for the prototype pixel detector is far above the theoretical expectation. To simulate crystallographic measurements under controlled conditions, the following 'mask' experiment was performed. A 0.2 mm thick tantalum mask with a square matrix of 0.2 mm diameter holes on 5 mm centres was moved to five different positions in front of the detector. Images of the holes were recorded with the detector at each position of the mask. After image correction (§2.2) the intensities of all spots were measured. The five intensities of each spot measured at the five mask positions were evaluated for mean and standard deviation. Spots contaminated by proximity to dead pixels were excluded from the analysis.

As discussed in §1.1, the standard deviation of an X-ray measurement follows equation (2). A factor  $\eta$  can be intro-

duced to compare the theoretical standard deviation with the standard deviation of experimental measurements:

$$\sigma(m) = \eta(m^{1/2}). \quad (11)$$

For a quantum limited detector, the factor  $\eta$  is unity. But the mask experiment verified that counting errors dominate measurements with the PILATUS 1M detector: the factor  $\eta$  is 7.5 for counting rates below  $1000 \gamma \text{ s}^{-1} \text{ pixel}^{-1}$  and increases for higher counting rates. The origin of this problem is fully understood and has been solved by a redesign of the readout chip. This PILATUS II chip has a special logic which prohibits counting errors. Measurements have shown that a pixel can count more than  $1.5 \times 10^6 \gamma \text{ s}^{-1} \text{ pixel}^{-1}$  without counting errors.

We thank M. Naef, H. Rickert, S. Streuli and F. Glaes of PSI for their help in fabrication of the PILATUS 1M detector, and C. Schulze-Briese, T. Tomizaki and C. Pradervand for their help in the experiments at beamline X06SA of the SLS. Many thanks are also owed to W. Kabsch for discussions and his help in processing our data with *XDS*. G. Hülsen acknowledges support from the Swiss National Science Foundation.

## References

- Arndt, U. W. (1986). *J. Appl. Cryst.* **19**, 145–163.
- Barna, S. L., Eikenberry, E. F., Gruner, S. M. & Tate, M. W. (1999). *Rev. Sci. Instrum.* **70**, 2927–2933.
- Broennimann, Ch., Bühler, Ch., Eikenberry, E. F., Horisberger, R., Hülsen, G., Schmitt, B., Schulze-Briese, C., Suzuki, M., Tomizaki, T., Toyokawa, H. & Wagner, A. (2004). *Synchrotron Radiat. News*, **17**, 23–30.
- Broennimann, Ch., Eikenberry, E. F., Henrich, B., Horisberger, R., Hülsen, G., Pohl, E., Schmitt, B., Schulze-Briese, C., Suzuki, M., Tomizaki, T., Toyokawa, H. & Wagner, A. (2006). *J. Synchrotron Rad.* **13**, 120–130.
- Brünger, A. T., Adams, P. D., Clore, G. M., DeLano, W. L., Gros, P., Grosse-Kunstleve, R. W., Jiang, J. S., Kuszewski, J., Nilges, M., Pannu, N. S., Read, R. J., Rice, L. M., Simonson, T. & Warren, G. L. (1998). *Acta Cryst.* **D54**, 905–921.
- Dauter, Z. & Wilson, K. S. (2001). *International Tables for Crystallography: Crystallography of Biological Macromolecules*, Vol. F, ch. 9.1.6.6. Dordrecht: Kluwer Academic Publishers.
- Diamond, R. (1969). *Acta Cryst.* **A25**, 43–55.
- Drenth, J. (1994). *Principles of Protein X-ray Crystallography*. Berlin: Springer Verlag.
- Evans, R. D. (1955). *The Atomic Nucleus*, p. 746. New York: MacGraw-Hill.
- Gemme, C. (2003). *Nucl. Instrum. Methods A*, **501**, 87–92.
- Gruner, S. M., Tate, M. W. & Eikenberry, E. F. (2002). *Rev. Sci. Instrum.* **73**, 2815–2842.
- Hülsen, G., Broennimann, Ch. & Eikenberry, E. F. (2005). *Nucl. Instrum. Methods A*, **548**, 540–554.
- Kabsch, W. (1988). *J. Appl. Cryst.* **21**, 916–924.
- Kabsch, W. (1993). *J. Appl. Cryst.* **26**, 795–800.
- Kabsch, W. (2005). Personal communication.
- Pflugrath, J. W. (1999). *Acta Cryst.* **D55**, 1718–1725.
- Plaisier, J. R., Koning, R. I., Koerten, H. K., van Roon, A. M., Thomassen, E. A., Kuil, M. E., Hendrix, J., Broennimann, C., Pannu, N. S. & Abrahams, J. P. (2003). *Nucl. Instrum. Methods A*, **509**, 274–283.
- Renzi, M. J., Tate, M. W., Ercan, A., Gruner, S. M., Fontes, E., Powell, C. F., MacPhee, A. G., Narayanan, S., Wang, J., Yue, Y. & Cuenca, R. (2002). *Rev. Sci. Instrum.* **73**, 1621–1624.
- Rossmann, M. G. (1979). *J. Appl. Cryst.* **12**, 225–238.
- Schnetzer, S. (2003). *Nucl. Instrum. Methods A*, **501**, 100–105.
- Schulze-Briese, C., Wagner, A. & Oetiker, M. (2005). *J. Synchrotron Rad.* **12**, 261–267.
- Sussman, J. L., Lin, D., Jiang, J., Manning, N. O., Prilusky, J., Ritter, O. & Abola, E. E. (1998). *Acta Cryst.* **D54**, 1078–1084.
- Wagner, A. (2006). In preparation.